Macromolecules **2003,** *36,* 749−758

SAXS and the Gas Transport in Polyether-*block*-polyamide Copolymer Membranes

Veroni Barbi,[†] Sergio S. Funari,[‡] Rainer Gehrke,[§] Nico Scharnagl,[⊥] and Norbert Stribeck*,[†]

Institute of Technical and Macromolecular Chemistry, University of Hamburg, Bundesstr. 45, 20146 Hamburg, Germany; Max-Planck-Institute of Colloids and Interfaces, c/o HASYLAB at DESY, Notkestr. 85, 22603 Hamburg, Germany; HASYLAB at DESY, Notkestr. 85, 22603 Hamburg, Germany; and GKSS Research Center, Postfach 1160, 21494 Geesthacht, Germany

Received August 16, 2002; Revised Manuscript Received November 20, 2002

ABSTRACT: Membranes from polyether-*block*-polyamide (PEBA) polymers with varying chemical composition (PEBAX), cast from 1-butanol and cyclohexanol, are studied by small-angle X-ray scattering (SAXS), dry and water-swollen, and as a function of strain. The nanostructure from soft and hard domains is determined. The typical hard domain thickness is 6 nm, and the long period is 17 nm for all grades. Gas transport parameters (permeability, diffusivity, solubility) are determined for He, H_2, CO_2, O_2, N_2, and CH_4. Increase of polyether domain thickness leads to an increased permeability, but imperfect microphase separation contributes to gas transport properties on the same order of magnitude. Utilizing the interface distribution function (IDF) and the multidimensional chord distribution function (CDF) analysis, we find that the nanostructure of PEBA materials with a high soft block content is hardly changed by variation of casting solvent or water content. Damage of the hard domains occurs during straining. The nanostructure of PEBA materials with a soft block content close to 50% ("balanced") is a function of the casting solvent. Membranes cast from cyclohexanol exhibit a decreased hard domain fraction caused from a declined phase separation. When the hard domains become too small, early failure upon straining is observed. One of the balanced materials exhibits an irregular domain structure; the other two form lamellar stacks with a different degree of order. Swelling in water is controlled by the chemical structure of the blocks. In the PEO/PA6 copolymer both soft and hard phase swell. The swellable PTMeO/PA12 copolymer shows growth of the soft domains only. Moderate elongation of the materials with a lamellar structure leads to orientation of the hard domain slabs parallel to the direction of strain. The extension of the slabs is <15 nm. Further elongation induces a microfibrillar structure with increasing heterogeneity. The most probable distance of two neighboring hard domains in the microfibril along the straining direction (long period) remains constant, but the shape of the long period distribution becomes skewed. When domains are destroyed during elongation, there is a tendency to form an orthorhombic macrolattice of almost spherical fragments in addition to the microfibrils.

Introduction

Gas permeation through a polymer membrane not only is a function of the chemical structure of the polymer chains but also is determined by a morphology inside the film with typical domain dimensions of several nanometers. Particularly in the case of membranes formed from block copolymers, such nanostructure may be varied considerably by modifying the type of the blocks, their length, and the materials processing. In the present study membranes from different commercial polyether-*block*-polyamide grades (PEBAX)[1] are characterized concerning both their nanostructure and gas transport properties.

The nanostructure of all PEBAX grades is built from polyamide (PA) hard domains dispersed in a soft matrix. In this soft phase the polyether blocks are predominating. As a function of an increasing fraction of hard domains, reduction of diffusivity and permeability is reported.[2,3] For polyurethane, imperfect nanophase separation is reported to hamper diffusion and to lower permeation.[4] For ethylene−propylene block copolymer membranes shape and orientation of the domains with respect to the film plane are related to the transport properties.[5] If in a membrane material bicontinuous topologies[6] can be formed crossing a percolation threshold, the permeation is reported to decrease considerably.[7]

For polymer membranes formed from stacks of lamellae, Premnath[8] proposes an advanced mathematical model for the permeability that considers the orientation distribution of the layers. Reciprocally, based on such a model, the fine structure of the permeation curve was used to draw conclusions on the morphology of the membrane.[9]

Nanostructure is frequently studied by transmission electron microscopy (TEM), atomic force microscopy (AFM),[10] and small-angle X-ray scattering (SAXS). Concerning the SAXS method, the amount of information on nanostructure that can be retrieved from the data increases with rising structural order. SAXS data from a heavily disordered membrane structure only permit to retrieve an average chord length[11] of domains. Increasing the amount of order, the chord distribution of domains or clusters in the membrane[12] was becoming accessible. With increasing correlation of the domains among each other, "long period peaks" were emerging in the scattering pattern. If the related structure is an ensemble of lamellar stacks, SAXS data are readily analyzed on the basis of the well-known notion of the interface distribution function.[13] In this study we ap-

---

[†] University of Hamburg.

[‡] Max-Planck-Institute of Colloids and Interfaces.

[§] HASYLAB at DESY.

[⊥] GKSS Research Center.

* Corresponding author: e-mail Norbert.Stribeck@desy.de.

10.1021/ma0213403 CCC: $25.00

Table 1. PEBAX Grades and Their Designation in This Study[a]

PEBAX grade	material designation	PEBAX grade	material designation
2533	80PTMeO/PA12	1074	55PEO/PA12
3533	70PTMeO/PA12	4011	57PEO/PA6
4033	53PTMeO/PA12		

[a] The first two digits in the label indicate the soft block weight fraction. In the sequel the soft and hard block polymers are identified. PTMeO = poly(tetramethylene oxide); PEO = poly(ethylene oxide); PA6 = polyamide-6; PA12 = polyamide-12.

plied this method to some of our data in order to determine the nanostructure of dry and water-swollen PEBA films. To the best of our knowledge, swelling of membranes has been studied[14−17] with less nanostructured materials only.

Moreover, order can be increased by orientating the membrane. In the anisotropic state, a multidimensional chord distribution[18,19] can be computed and analyzed to retrieve information on domain shape and arrangement. Unless the hard domains are destroyed[20,10] during straining, conclusions on the nanostructure in the isotropic state can be drawn. Comparing the determined morphological data to the gas permeation process parameters, we thus intend to assess the effect of the polymer nanostructure to gas transport.

Experimental Section

Materials and Membrane Preparation. Five commercial grades of polyether-*block*-polyamide copolymers (PEBA) (PEBAX, Elf Atochem Inc.) with varying soft block fraction and varying chemical composition were selected (cf. Table 1). Solvent-free films of 50−200 μm thickness were prepared by solution-casting from two different solvents (1-butanol and cyclohexanol). Solutions (4 wt %) were obtained after approximately 30 h reflux at temperatures close to the boiling points of the solvents and vigorous stirring, then cast on Teflon-coated glass plates at 40 °C, and finally dried in two steps. The last step was performed in a vacuum at elevated temperature (60−70 °C for 12 h).

Characterization of Gas Transport Properties. Gas transport properties of the membranes were determined in time-lag experiments using a vacuum time-lag apparatus built by S. Shishatskii at GKSS, Geesthacht. Before the measurement each membrane was allowed to rest in the evacuated apparatus for at least 12 h. Pure gases were applied at feed pressures below 1 bar. Permeate pressure increase with time, $p_p(t)$, was recorded at 30 °C by two MKS Baratron pressure sensors. Typically, the total time of measurement was set to four time lags. Time lags, Θ, below 1 s can be measured and reproduced with high precision. Permeate pressure was $<10^{-4}$mbar at the beginning of the experiment and was recorded up to 0.05−9 mbar, depending on the feed gas. The permeability, P, was calculated from the slope of the curve $p_p(t)$ in the steady-state region for several feed gas pressures and extrapolated to a feed gas pressure of zero. Apparent diffusion coefficients, D_a, were estimated from the average time lag, $\bar{\Theta}$, using the relation $D_a = \bar{\ell}^2/6\bar{\Theta}$ ($\bar{\ell}$ being the average membrane thickness). Apparent solubility coefficients, S_a, were calculated from $S_a = P/D_a$. The thickness of the membrane was measured at 10 different spots. Every time-lag measurement was carried out three times, thus providing statistical data to estimate the propagated error of determination.

SAXS Experiments. Small-angle X-ray scattering (SAXS) experiments were performed in the synchrotron beam line A2 at HASYLAB, Hamburg, Germany. The wavelength of the X-ray beam was 0.15 nm. SAXS images were collected by a two-dimensional position-sensitive CCD detector (MAR 185; 2048 × 2048 pixels of 0.079 × 0.079 mm^2). The sample-to-detector distance was set to 1620 mm. The minimal accessible scattering angle corresponded to a d spacing of 33 nm. The maximal scattering angle corresponded to 2.8 nm. The flux of the attenuated primary beam was measured using a pin diode in the beam stop. Sample strips (40 × 12 mm^2) with elongational marks were mounted in a straining stage (courtesy of B. Heise, University of Ulm, Germany) positioned in the synchrotron beam, slowly strained up to the chosen true elongation, and exposed for 2−20 min. Saturation of the samples swollen in water (12 h) was confirmed.

SAXS Data Evaluation. Images were normalized with respect to the incident flux, and blind areas were masked. The instrument background was subtracted considering sample absorption. The center and orientation of the patterns were determined. The patterns were aligned and averaged with respect to the four quadrants. As the final step in image preprocessing, remnant blind spots were filled utilizing a two-dimensional extrapolation based on radial basis functions.[21]

Data processing was performed similar to the procedure described in earlier work.[18,22] Unstrained samples proved to be isotropic. From these patterns scattering curves were extracted. If discrete SAXS was observed, the interface distribution function (IDF), $g_1(r)$, was computed. An analysis by fitting a one-dimensional (1D) paracrystalline stack of layers was attempted. Strained samples exhibiting discrete and anisotropic scattering were processed to yield the 3D chord distribution, $z(r_{12},r_3)$, with cylindrical symmetry. The positions of maxima and minima in $z(r_{12},r_3)$were determined. On the basis of these data, conclusions on the nanostructure were drawn.

In detail, the preprocessed anisotropic images were projected onto the fiber plane and multiplied by s^2, and a preliminary background was subtracted. Here $\mathbf{s} = (s_{12},s_3)$ is the scattering vector in cylindrical coordinates with its modulus $s = |\mathbf{s}| = (2/\lambda) \sin \theta$, where λ is the wavelength of X-radiation and and 2θ is the scattering angle. Differing from previous treatment this background was not considered a constant, but a biquadratic polynomial ($b(s_{12},s_3) = c_0 + c_{12}s_{12}{}^2 + c_3s_3{}^2$). Its coefficients were determined by regression from the trailing region of the pattern. This procedure is both closer to the common notion of the SAXS background and even capable of removing warped backgrounds that had been observed in some cases. The remnant background to be subtracted was constructed by iterative spatial frequency filtering. Well-balanced interference functions of the two-phase nanostructure, $G(s_{12},s_3)$, were obtained after four iterations. These functions finally underwent a 2D Fourier transformation, resulting in a multidimensional chord distribution function (CDF) of the nanostructure. The interpretation of this function is straightforward, since the CDF has been defined[18] by the Laplacian of Vonk's multidimensional correlation function.[23] As such, it presents the autocorrelation of the surfaces from the (nanosize) domains in space in a similar manner as Ruland's interface distribution function does[13,24,25] for one-dimensional structures as a function of distance. For samples with fiber symmetry the CDF $z(r_{12},r_3)$ is a function of two coordinates only (transverse direction r_{12} and the fiber direction r_3). Therefore, it can be displayed by means of contours or density plots in a plane. Positive peaks found in the vicinity of the origin are size distributions of the primary domains. Thus, their size, shape, and orientation in space are depicted. Negative peaks following farther out exhibit “long periods”, i.e., the distance of two adjacent domains from each other. Positive peaks following next describe the size and orientation of superdomains (i.e., clusters made from two adjacent domains), and correlations among domains more distant are manifested in consecutive peaks at even longer distance.

Isotropic data, as well, were treated by spatial frequency filtering in order to extract the nanostructure information as has been described elsewhere.[22,26] Because of apparent domain surface roughness, an iterative filter (three iterations) was applied.

To detect distortions that may be caused from the iterative application of the spatial frequency filter, both noniterated curves and noniterated anisotropic patterns were processed in addition and compared to the iterated IDFs and chord length distributions. In general, the noniterated results were

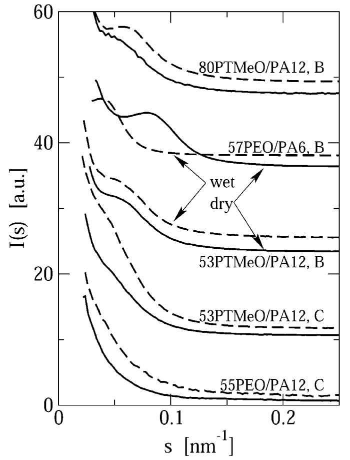

Figure 1. SAXS of neat PEBA films (unstrained, isotropic). Dry (solid lines) and after swelling in water for 12 h (broken lines). Different PEBA grades solvent-cast from 1-butanol (B) and cyclohexanol (C). The curves are shifted for clarity.

found to be identical to the functions found in the iterative process, except for a strong "roughness" peak at the origin. Therefore, the iterated results were accepted. Differences between iterated and noniterated results were observed for all the isotropic data from material 70PTMeO/PA12. The consequences will be discussed in the corresponding subsection of the results.

For each of the curves from the isotropic samples the invariant $Q = \int s^2 I(s)\,ds$ was determined in order to estimate a changing density difference between the hard and the soft phase.

Results and Discussion

SAXS of Unstrained Samples. For the unstrained, isotropic films some of the measured SAXS curves are shown in Figure 1. Curves from water-swollen samples are indicated by dashed lines. Most of the curves exhibit a long period reflection that is characteristic for correlation among domains in a multiphase system. In general, this discrete SAXS is decreasing as a function of increasing polyamide content, except for 55PEO/PA12 which shows extremely weak scattering. Water-swollen materials show a more pronounced long period peak. A considerable shift of the peak position is only observed for the 57PEO/PA6 material. By swelling in water it becomes a gel that cannot be strained any more.

To analyze the nanostructure of isotropic data quantitatively, we assume the morphology of a layer system, transform the measured data, and finally fit them using a lamellar 1D model.[27,28] If the assumption is not justified, it can often be detected from the fact that the 1D model does not fit. Quantitative data evaluation of the isotropic data starts with the computation of the one-dimensional interference function, $G_1(s)$. The top curve in Figure 2 shows raw scattering data after multiplication by s.^{4} Here a linear Porod region is clearly visible in the interval $0.15\ \mathrm{nm}^{-1} < s < 0.22\ \mathrm{nm}^{-1}$. After three iterations of the spatial frequency filter an interference function, $G_1(s)$, is returned (bottom curve, solid line). After 1D Fourier transformation the interface distribution function, $g_1(r)$, is obtained (Figure 3, circles). In the drawing the fit of this function by a 1D stacking model is indicated by a solid line. The fits of curves related to the material 80PTMeO/PA12 show poor quality, whereas the fits of the samples with an almost balanced composition of polyether and polyamide show a good quality (cf. Figure 3). For 80PTMeO/PA12 a good fit cannot be expected because of the fact that its composition does not favor the formation of a lamellar system.

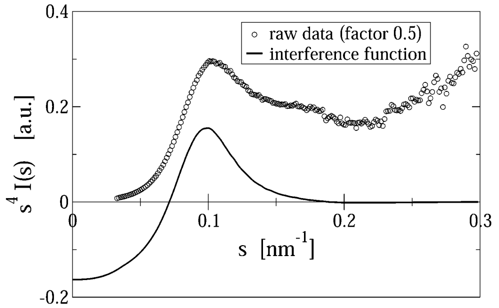

Figure 2. Example for the extraction of the interference function $G_1(s)$ (solid line) by spatial frequency filtering from the SAXS raw data (open symbols). A constant background is subtracted from the raw data before multiplication by s^4, chosen to linearize the Porod region.

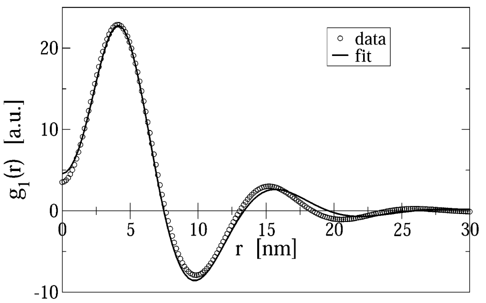

Figure 3. Interface distribution (IDF) $g_1(r)$ (open symbols) is computed by 1D Fourier transformation from $G_1(s)$ and fitted to a model of stacked lamellae (solid line).

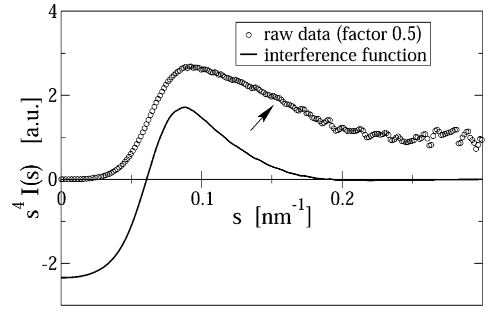

Figure 4. 70PTMeO/PA12,C, dry. Automatic extraction of the interference function $G_1(s)$ (solid line) by spatial frequency filtering from the SAXS raw data (open symbols).

The material 70PTMeO/PA12 takes an intermediate position (cf. Figure 4). For all its samples a manual determination of $G_1(s)$ yields a different result than the spatial frequency filtering method. The manual result cannot be fitted by a simple layer stack model, but the filtered result can. The reason is in the different handling of the region that is indicated by an arrow. The filter applied to the relatively smooth shape of this SAXS obviously removes too much background from the curve and generates an interference function (solid line) that can be fitted.

Fit results are parameter values describing the lamellar nanostructure in terms of the average layer thicknesses and the widths of the layer thickness distributions in the stacks (Table 2). The association of layer thicknesses to the two phases has been guessed from the known composition of the block copolymer and the notion that hard domains (polyamide) should be somewhat more perfect in order to keep them stable.

Table 2. Lamellar Nanostructure of Isotropic PEBA Membranes As Determined by SAXS IDF Analysis[a]

	53PTMeO/PA12		57PEO/PA6		70PTMeO/PA12	
	dry	wet	dry	wet	dry	wet
			Cast from 1-Butanol			
$\bar{t}_E$ [nm]	6.9 ± 0.5	7.0 ± 0.5	5.7 ± 0.2	10.5 ± 0.4	7.2 ± 0.2	7.1 ± 0.2
$\bar{t}_A$ [nm]	6.0 ± 0.4	6.0 ± 0.3	4.6 ± 0.2	7.5 ± 0.2	5.1 ± 0.1	5.2 ± 0.1
$\sigma_E/\bar{t}_E$	0.59 ± 0.03	0.58 ± 0.04	0.46 ± 0.05	0.44 ± 0.04	0.52 ± 0.03	0.52 ± 0.03
$\sigma_A/\bar{t}_A$	0.44 ± 0.05	0.35 ± 0.04	0.46 ± 0.04	0.47 ± 0.02	0.42 ± 0.02	0.41 ± 0.02
			Cast from Cyclohexanol			
$\bar{t}_E$ [nm]	8.2 ± 0.3	8.3 ± 0.3	5.8 ± 0.2	9.1 ± 0.4	7.0 ± 0.2	7.1 ± 0.2
$\bar{t}_A$ [nm]	5.5 ± 0.1	5.3 ± 0.1	4.1 ± 0.1	6.0 ± 0.2	5.1 ± 0.1	4.8 ± 0.1
$\sigma_E/\bar{t}_E$	0.65 ± 0.08	0.51 ± 0.02	0.51 ± 0.02	0.50 ± 0.04	0.51 ± 0.02	0.51 ± 0.03
$\sigma_A/\bar{t}_A$	0.42 ± 0.07	0.31 ± 0.04	0.45 ± 0.02	0.44 ± 0.04	0.42 ± 0.03	0.42 ± 0.03

[a] $\bar{t}_E$, $\bar{t}_a$ = average layer thicknesses of polyether and polyamide phase, Respectively. $\sigma_E/\bar{t}_E$, $\sigma_A/\bar{t}_A$ = observed relative widths of the layer thickness distributions of polyether and polyamide phase, respectively.

Table 3. Relative Change of the SAXS Invariant, *Q*, after Replacing the Casting Solvent 1-Butanol by Cyclohexanol

material	Q_{cy}/Q_{bu}	material	Q_{cy}/Q_{bu}
80PTMeO/PA12	0.70	55PEO/PA12	0.96
70PTMeO/PA12	0.84	57PEO/PA6	0.42
53PTMeO/PA12	0.84		

We determine layer thicknesses that are on the order of 6 nm and average long periods, $\bar{L} = \bar{t}_E + \bar{t}_A$, ranging from 12 to 18 nm. For dry films having a balanced composition of hard and soft blocks cast from 1-butanol, we compute polyether domain volume fractions, $\phi_E = \bar{t}_E/\bar{L}$, that are very close to the polyether weight fractions in the block copolymers. After saturating the materials with water, the average layer thicknesses of 53PTMeO/PA12 have not changed. Only a tendency to narrow the polyamide layer distribution can be observed. 57PEO/PA6, on the contrary, exhibits a considerable swelling of the lamellar nanostructure. Both kinds of layers swell by the same factor. Thus, the volume fraction of soft domains is changing little.

53PTMeO/PA12 cast from cyclohexanol exhibits a different nanostructure than that observed with the same material when cast from 1-butanol. The long period is slightly enhanced by 1 nm, but the volume fraction of the soft phase has increased from $\phi_E = 0.53$ to $\phi_E = 0.60$. The polyamide hard domains have become considerably smaller. Swelling, again, narrows the layer thickness distributions. Here both the polyether and the polyamide thickness distributions are affected.

70PTMeO/PA12 evaluated under the assumption of a layer system shows little variation of the nanostructure as a function of both casting solvent and water content. The soft phase fraction $\phi_E \approx 0.6$ computed from the fit parameters is considerably lower than the value expected from the composition of the material. This is another indication that the model of a lamellar system appears to be inappropriate for this sample. Thus, for this material the reported "layer thicknesses" should not be compared with other materials or the results of other methods. Their constancy only confirms that the method of preparation does not change size and arrangement of the domains in this material.

Replacing the casting solvent 1-butanol by cyclohexanol causes a reduction of the scattering power *Q* for all PEBA materials. The corresponding reduction factors are reported in Table 3. Because we do not know the corresponding change of the fraction of the soft domains, we cannot compute a change of the density contrast between soft and hard phase. Nevertheless, from the data it becomes clear that a considerable change of contrast may occur. In particular, for our membranes 80PTMeO/PA12 and 57PEO/PA6 we assume that the phase separation of the membranes cast from cyclohexanol is considerably reduced as compared to the membranes cast from 1-butanol.

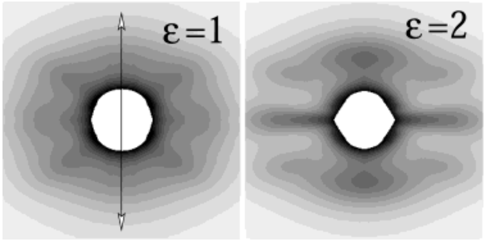

Figure 5. SAXS intensity $I(s_{12},s_3)$ ($-0.1\ \text{nm}^{-1} \leq s_{12}, s_3 \leq 0.1\ \text{nm}^{-1}$) as a function of elongation ϵ. 80PTMeO/PA12 film cast from 1-butanol. Water swollen. The straining direction (s_3) is indicated.

SAXS of Strained Samples. a. 80PTMeO/PA12. Figure 5 demonstrates the SAXS of the material 80PTMeO/PA12 as a function of elongation $\epsilon = (\ell - \ell_0)/\ell_0$, with ℓ_0 and ℓ defined by the initial length and the actual length, respectively. Data of the neat material before straining were already presented in Figure 1. The straining direction is indicated by a double head arrow. The two patterns are representative for all the samples of this material what the obvious features of the SAXS patterns are concerned. Several peaks only observed close to the center of the pattern indicate a nanostructure with some short-range order. More information concerning this morphology can be extracted from the chord distribution function (CDF) $z(r_{12},r_3)$ (Figure 6). The upper drawing shows the CDF viewed from the top. The strong ring-shaped peak ("a-peak") in the center indicates that the basic domain is an almost spherical ellipsoid. The four peaks surrounding the central ring indicate the distributions of chords made from a domain diameter, a gap formed from matrix material and another domain diameter ("aba-peaks"; different letters in the term "aba" indicate each one of the two phases). Each pair of these peaks is separated by a deep valley at the meridian that is caused from a strong and narrow, ridge-shaped long period peak on the meridian of the CDF. Because of the fact that the lateral extension of such a pair does not extend beyond the lateral extension of the central ring peak, we hesitate to describe this morphology by the notion of a central sphere surrounded by four neighbors. Instead, it appears more probable that we observe a two-component structure with different range of order. An orthorhombic macrolattice of ellipsoids in a matrix forms the compo-

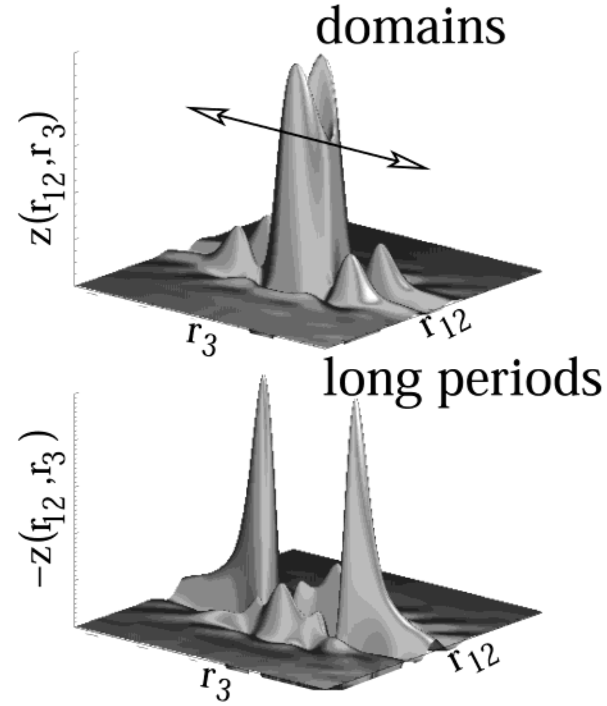

Figure 6. Nanostructure revealed in the multidimensional chord distribution, $z(r_{12},r_3)$ (-50 nm $\leq r_{12}$, $r_3 \leq 50$ nm), as computed from the SAXS. PEBA film 80PTMeO/PA12 cast from 1-butanol, water swollen, at an elongation $\epsilon = 2$. Top: chord distribution viewed from the top. Bottom: chord distribution turned upside down. The straining direction is indicated.

nent with the longer range of order (i.e., with bigger "single crystals" of colloidal dimension). The component with a shorter range of order is a distorted nanofibrillar system extending along the straining direction. The lateral extension of its correlation volume[29] is rather narrow and thus causes the splitting of the broad aba-peaks about the meridian.

The lower plot shows the same function viewed from the bottom side. Long period peaks are observed here. We find that in straining direction the long period distribution is skewed seriously. Most of the chords made from one domain thickness plus one matrix thickness (ab-peaks) are rather short, but there are considerable amounts of such distances that are much longer. Further long period peaks are observed that are not placed on the meridian and indicate the above-mentioned orthorhombic macrolattice.[30] Their shape is less skewed.

Figure 7 presents contours that show elevations of $z(r_{12},r_3)$ with respect to its zero level as a function of elongation and water content for the samples cast from 1-butanol. The corresponding plots for films cast from cyclohexanol look similar. The plots at an elongation of $\epsilon = 1$ exhibit that water-swollen samples show a higher lateral correlation among the domains than the dry materials. At $\epsilon = 2$ the lateral correlation for both samples is low, and the contour plots are rather similar for both the dry and the water-swollen sample. More significant differences are found in the corresponding "negative" contours that mark depressions in $z(r_{12},r_3)$ below its zero level, as presented in Figure 8. At $\epsilon = 2$ we observe that there is still some lateral correlation among the ellipsoids, although the orthorhombic macrolattice now appears to be somewhat distorted as well. Not only have the equatorial peaks moved toward the center but also have the off-axis peaks decreased and moved toward the strong long period ridge that has developed on the meridian. In the case of the dry material the off-axis peaks have already merged with the contours of the ridge.

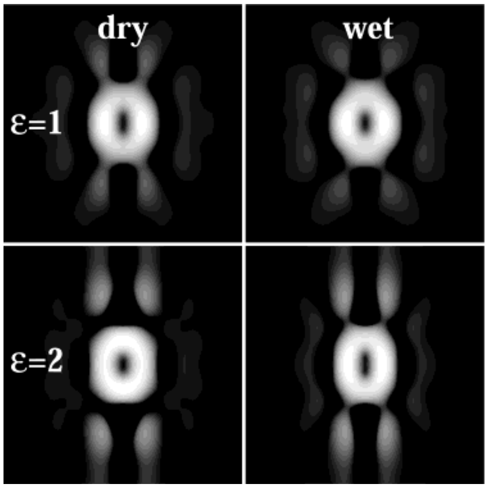

Figure 7. 80PTMeO/PA12. Positive peaks ("domains", logarithmic scale) of the multidimensional chord distribution $z(r_{12},r_3)$(-40 nm $\leq r_{12}$, $r_3 \leq 40$ nm) as a function of elongation and water content.

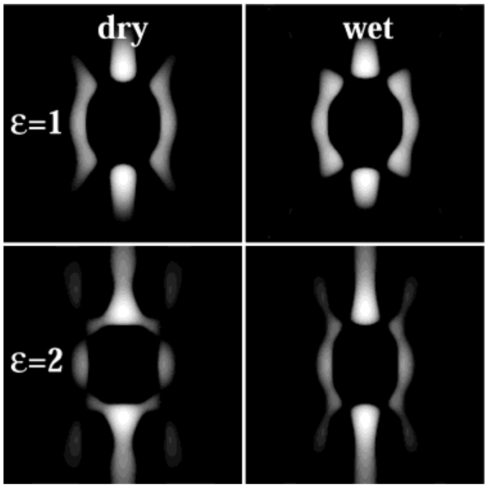

Figure 8. 80PTMeO/PA12. Negative peaks ("long periods", logarithmic scale) of the multidimensional chord distribution $z(r_{12},r_3)$(-40 nm $\leq r_{12}$, $r_3 \leq 40$ nm) as a function of elongation and water content.

Considering the positions of all peaks in the CDF, we can extract information concerning the shape and mutual arrangement of the domains with respect to the straining direction. As long as no multidimensional model of the distorted nanostructure is available that can be fitted to the CDF, this method is the only way to understand the morphology.

Table 4 reports the position of the domain ring maximum in meridional direction, $\langle t_m \rangle$ ("domain height"), determined from the positive face of the chord distribution and the aspect ratio of the domain ring, $\langle t_m \rangle / \langle t_e \rangle$, as a function of elongation and water content. We observe an increase of both the domain height and the aspect ratio as a function of elongation. This can be explained by different notions: (1) the domains originally are spheres that show a certain elasticity; (2) the domains degrade during elongation; (3) the domains are already anisotropic in the isotropic sample and orient owing to

Table 4. 80PTMeO/PA12 Domain Shape Data as a Function of Elongation ϵ and Water Content[a]

	dry			wet		
ϵ	$\langle t_m \rangle$ [nm]	$\langle t_m \rangle/\langle t_e \rangle$	V_ϵ/V_0	$\langle t_m \rangle$ [nm]	$t_m \rangle/\langle t_e \rangle$	V_ϵ/V_0
0	7.2 ± 0.2	1	1	7.0 ± 0.2	1	1
1	8.2 ± 0.2	1.3	0.92	7.8 ± 0.2	1.2	0.99
2	8.1 ± 0.2	1.3	0.88	8.2 ± 0.2	1.4	0.80

[a] $\langle t_m \rangle$ = most probable domain height in meridional direction. $\langle t_m \rangle/\langle t_e \rangle$ = domain aspect ratio. V_ϵ/V_0 = relative change of domain volume.

strain. Let us try to identify the most probable process. Initial anisotropy should result in a strong increase of $\langle t_m \rangle$ while the decrease of $\langle t_e \rangle$ is only moderate, because the average chord length of an anisotropic particle is closer to its minimum diameter than to its maximum diameter. Such behavior is not observed. Another hint can be gained by considering the domain volume variation, V_ϵ/V_0. The domain volume can be computed by $V = \langle t_e \rangle^2 \langle t_m \rangle$ (cf. Table 4). There should be no change for perfect rubber elasticity. At least the values computed for the wet sample indicate elastic deformation of spherical domains with an initial diameter of 7 nm. Orientation of anisotropic domains that remain intact can be excluded. An indication for the destruction of domains concerning the dry materials can be extracted from the progression of the most probable long period $\langle L \rangle$, as compared to the increase of the most probable domain height, $\langle t_m \rangle$. The absolute increments of both lengths are identical, and we conclude that the virtual increase of both quantities can be explained by a process in which small and imperfect domains are destroyed, as has been found in similar studies on block copolymers containing polyether and polyester ("PEE").[31]

To identify the domains just described, we now consider the maximum positions $\langle L \rangle$ of the long period peaks of the isotropic patterns in the CDF. For the dry sample we find $\langle L \rangle = 17.2$ nm. The wet sample shows its maximum at $\langle L \rangle = 16.0$ nm. Relating these lattice constants to the 7 nm domain diameters and considering the weight composition of the block copolymer (20% PA12), we thus attribute the domain peak found in the CDF to the PA12 hard domains from the materials. Moreover, this assignment is supported by findings of an AFM study on the similar 70PTMeO/PA12 reporting long periods of 16 nm and domain diameters of 6 nm.[10]

Comprising the results of nanostructure analysis, the strained material 80PTMeO/PA12 contains slightly anisotropic hard domains of approximately 8 nm height and 6 nm diameter. The variation of the SAXS as a function of elongation indicates a moderate destruction of hard domains as a result of straining the material. There is a strong microfibrillar component, in which those domains are lined up parallel to the direction of strain. Its most probable long period is 17 nm and does not change as a function of strain. Instead, the shape of the distribution is changed, indicating that a majority of the mesh lengths resist whereas an increasing minority is extended by varying amounts. Additionally, a considerable amount of hard domains shows correlation with domains perpendicular to the direction of strain. Those correlated assemblies form a distorted orthorhombic macrolattice with a lattice constant of approximately 13 nm in equatorial direction at $\epsilon = 1$ that is decreasing to 11 nm upon straining to $\epsilon = 2$.

Samples cast from both 1-butanol and cyclohexanol show almost the same two-phase topology. Swelling in water causes small changes, but only what the hard domain size is concerned. The inherent inhomogeneity of the strained nanostructure is decreased in the water-swollen samples.

b. 70PTMeO/PA12. The general features in the SAXS patterns and in the CDFs of the strained material are very similar to the corresponding data of dry 80PTMeO/PA12. Also, the patterns from the strained samples show that the fundamental nanostructure is altered neither by the casting solvent nor by swelling the material in water. In the elongated state the domains appear to be elongated ellipsoids with a constant aspect ratio $\langle t_m \rangle/\langle t_e \rangle = 1.3$, which is similar to the average aspect ratio found with the 80PTMeO/PA12 material. At $\epsilon = 1$ the most probable domain height determined from the CDFs is $\langle t_m \rangle = 8.3$ nm for all samples except for the wet sample cast from 1-butanol (8.0 nm).

With domain diameters between $\langle t_e \rangle = 6.2$ nm for the wet 1-butanol sample and 6.9 nm for the wet cyclohexanol sample and 6.5 nm for both dry samples, our CDF analysis thus confirms the values that have been found by AFM for the hard domain diameters in a study of the same material by McLean and Sauer.[10] McLean and Sauer report that SAXS data from a correlation function analysis yield hard domain diameters that are by 2 nm smaller than the diameters found by AFM. Similar reduction has been found by us using a fit of the IDF (cf. Table 2, parameter $\bar{t}_A$). This finding can be explained by the fact that both the correlation function method and the IDF analysis apply an inappropriate layer stack model to a material containing domains that are no lamellae. As has been pointed out by the authors of the cited study, these domains are destroyed upon straining. Thus, the "sausage-shaped" domains observed by McLean and Sauer cannot be visualized by our method.

McLean and Sauer report long periods of 16 nm for the isotropic sample and 17 ± 3 nm for all the strained samples, independent of elongation. Determined from the minima in the CDF all our unstrained samples show the same long period of $L = 16.8$ nm. At $\epsilon = 1$ we find $L_m = 17.8$ nm for the samples cast from 1-butanol and $L_m = 18.2$ nm for the samples cast from cyclohexanol. L_m is the long period peak on the meridian of the CDF.

Severe damage of nanostructure is only observed with the 70PTMeO/PA12 material at $\epsilon = 2$. The most probable domain heights and the corresponding long periods in straining direction decrease for all samples. The wet samples show a moderate decrease of these parameters by approximately 2%. For the dry sample cast from cyclohexanol the corresponding decrease is 8%. The dry sample cast from 1-butanol does not show discrete SAXS any more when strained to $\epsilon = 2$, although there is no macroscopic failure. Here there are no correlated domains any more.

c. 57PEO/PA6. In water this material swells significantly. Moreover, the films cast from cyclohexanol break early when they are strained. Thus, there are only data from the dry film cast from 1-butanol.

Figure 9 shows the central part from the scattering patterns taken at $\epsilon = 1$ and 2. At both elongations we observe a SAXS two-point pattern with its maxima on the equator. Such patterns are frequently addressed to indicate a nematic structure. The CDFs presented in Figure 10 show that here such an interpretation would be incorrect. Instead, a lamellar system with a peculiar orientation is observed. In the positive contours two

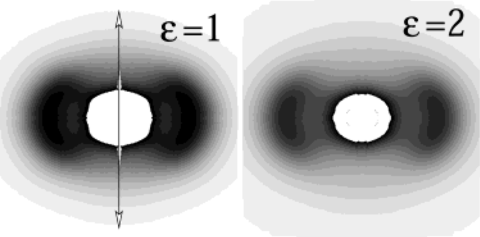

Figure 9. SAXS intensity $I(s_{12},s_3)$ (-0.15 nm^{-1} $\leq s_{12}$, $s_3 \leq 0.15$ nm^{-1}) as a function of elongation ϵ. 57PEO/PA6 film cast from 1-butanol. The straining direction (s_3) is indicated.

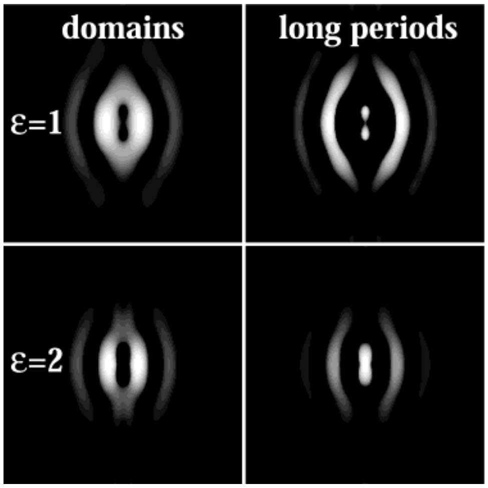

Figure 10. 57PEO/PA6. Density plots in logarithmic scale of the multidimensional chord distribution $z(r_{12},r_3)$ (-40 nm $\leq r_{12}$, $r_3 \leq 40$ nm) as a function of elongation.

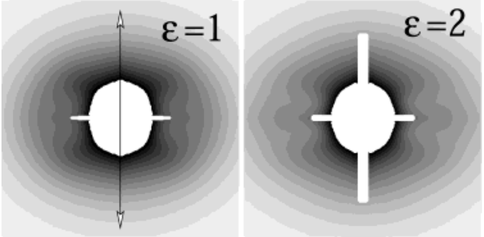

Figure 11. SAXS intensity $I(s_{12},s_3)$ (-0.1 nm^{-1} $\leq s_{12}$, $s_3 \leq 0.1$ nm^{-1}) as a function of elongation ϵ. 53PTMeO/PA12 film cast from 1-butanol. The straining direction (s_3) is indicated.

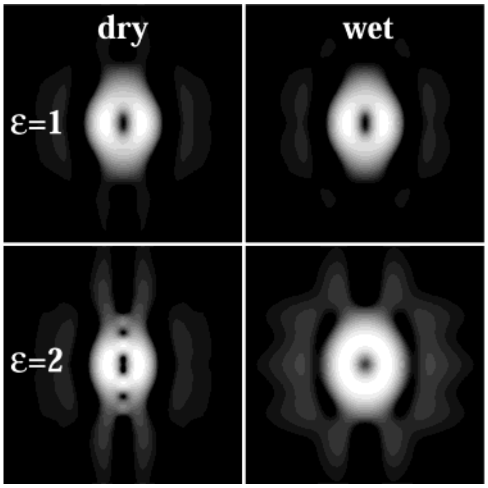

Figure 12. 53PTMeO/PA12. Positive peaks ("domains", logarithmic scale) of the multidimensional chord distribution $z(r_{12},r_3)$(-40 nm $\leq r_{12}$, $r_3 \leq 40$ nm) as a function of elongation and water content for the samples cast from 1-butanol.

strong and elongated peaks on the equator exhibit the basic domain: a layer oriented parallel to the direction of strain. Further out on the equator, even two rather strong "aba" domain peaks are extending parallel to the meridian. At $\epsilon = 1$ the lateral extension of this pair of layers is larger than 15 nm, and at $\epsilon = 2$ it is still well beyond 10 nm. Such an extended correlation perpendicular to the direction of orientation appears contradictory to the common notion of a nematic structure. The negative contours show the long periods ("ab" peaks). In particular, at $\epsilon = 1$ we observe a superposition of two components. The first is related to long periods of lamellae that are aligned parallel to the straining direction. The second comprises layers that are tilted. The tilt angle is 27°. The weak contribution of the tilted lamellae to the "aba" peaks indicates that the thickness of the second tilted lamella in each pair is poorly defined. The most probable lamellar thickness ($\langle t\rangle_{\mathrm{e},\epsilon=1} = 5.8$ nm, $\langle t\rangle_{\mathrm{e},\epsilon=2} = 5.1$ nm) is half the long period ($\langle L\rangle_{\mathrm{e},\epsilon=1} = 11.8$ nm, $\langle L\rangle_{\mathrm{e},\epsilon=2} = 10.3$ nm), corresponding to the composition of the material. The observed reduction at the higher elongation is explained by the compressibility of the soft polyether layers.

Comprising the results of the nanostructure analysis, the 57PEO/PA6 material forms lamellar stacks with a short-range order that is comparable to many semicrystalline polymers. Straining the membrane results in an orientation of the layers parallel to the direction of strain. This results in a SAXS pattern that, at the first glance, resembles a nematic pattern. Nevertheless, in the CDF the lamellar nanostructure is revealed. It is related to the rapid falloff of the scattering intensity in meridional direction. Nanostructure is strongly affected by the choice of the casting solvent. The small hard domains formed when casting from cyclohexanol may be the reason for the observed poor mechanical properties.

d. 53PTMeO/PA12. Figure 11 shows the central part from the scattering patterns taken at elongations $\epsilon = 1$ and 2. At both $\epsilon = 1$ and $\epsilon = 2$ we observe a complex SAXS pattern with a very broad pair of layer lines parallel to the equator, and the two-point pattern on the equator that has been found with the other materials as well. Positive contours of the CDFs are presented in Figure 12 for the films cast from 1-butanol. The positive contours for the samples cast from cyclohexanol look similar, but the lateral extension of their layers is considerably larger. Only the plot of the dry sample at $\epsilon = 2$ looks completely different. It does not show the splitting of domain peaks demonstrated in the bottom left graph of Figure 12.

At $\epsilon = 1$ we observe very strong and broad domain scattering peaks that differ little from the layer peaks observed with 57PEO/PA6. The most probable layer thickness $\langle t\rangle_{\mathrm{e},\epsilon=1}$ is independent of the water content (6.2 nm for the 1-butanol and 6.6 nm for the cyclohexanol sample). The vertical extension of the peaks on the equator can be considered a measure for the extension of the layers. We observe a reduction with the water-swollen sample. Such a reduction is not observed for the material cast from cyclohexanol.

At $\epsilon = 2$ the dry sample cast from 1-butanol shows many peaks that can be attributed to fragments of the initial layers with some short-range order. The most probable layer thickness is decreased to $\langle t\rangle_{\mathrm{e},\epsilon=2} = 5.1$ nm. For the wet samples, on the other hand, we observe an increase to $\langle t\rangle_{\mathrm{e},\epsilon=2} = 7.0$ nm and an isotropization of

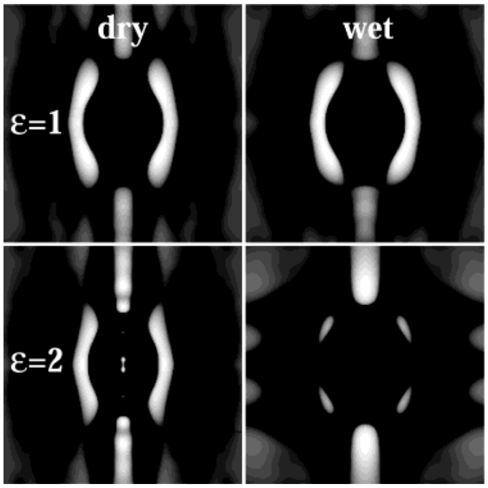

Figure 13. 53PTMeO/PA12. Negative peaks ("long periods", logarithmic scale) of the multidimensional chord distribution $z(r_{12},r_3)$(-40 nm $\leq r_{12}, r_3 \leq 40$ nm) as a function of elongation and water content. The negative contours are very weak.

the positive CDF contour pattern. Moreover, we find a considerable decrease of scattering intensity between $\epsilon = 1$ and $\epsilon = 2$. Thus, we conclude that the lamellae are extinguished or transformed into ellipsoidal domains. Similar domains were found in 80PTMeO/PA12.

The negative contours are presented in Figure 13. They, indeed, look similar to the corresponding contours from 80PTMeO/PA12 and have to be addressed as the contours of lattices made from spherical particles. What is the reason that we do not see the spheres on the positive face of the CDF? We have to consider the strength of the peaks. In the most favorable case (wet, $\epsilon = 2$) the ratio of the peak heights from positive and negative face is 1/20. For all the others it is even smaller than 1/100. Thus, in the strained state the CDFs describe, more or less, domains without arrangement. Only a small fraction of the domains is arranged. The shape of the latter can be described by ellipsoids, whereas the majority of the domains can be described by imperfect layers, arranged at random but with a tendency to orient under strain. Films cast from cyclohexanol exhibit an even poorer arrangement of domains.

Comprising the results of the analysis of the strained state, the 53PTMeO/PA12 material forms imperfect layers that are poorly arranged. When cast from 1-butanol, the lamellae are more compact. Moreover, a small fraction of the material forms a morphology that already has been found with the 80PTMeO/PA12. This small fraction can be described by a lattice of almost spherical particles with short-range order. Straining leads to a peculiar orientation of the layers that already was observed with the 57PEO/PA6. Swelling in water does not severely affect the structure of the sample cast from cyclohexanol, but it appears to shrink the lateral extension of the layers. Lamellae fail at high elongation. The failure mechanism is both a function of casting solvent and water content.

e. 55PEO/PA12. This material shows extremely weak scattering only. Apart from central particle scattering no peaks can be seen in the measured data. Thus, nanostructure parameters that may be related to gas transport properties should not be determined. Nevertheless, after severe smoothing by a median filter, scattering peaks are observed (cf. Figure 14). Because of the weakness of the scattering patterns, we hesitate to discuss them in detail, but the features are comparable to those of the other materials having a balanced composition of hard and soft blocks.

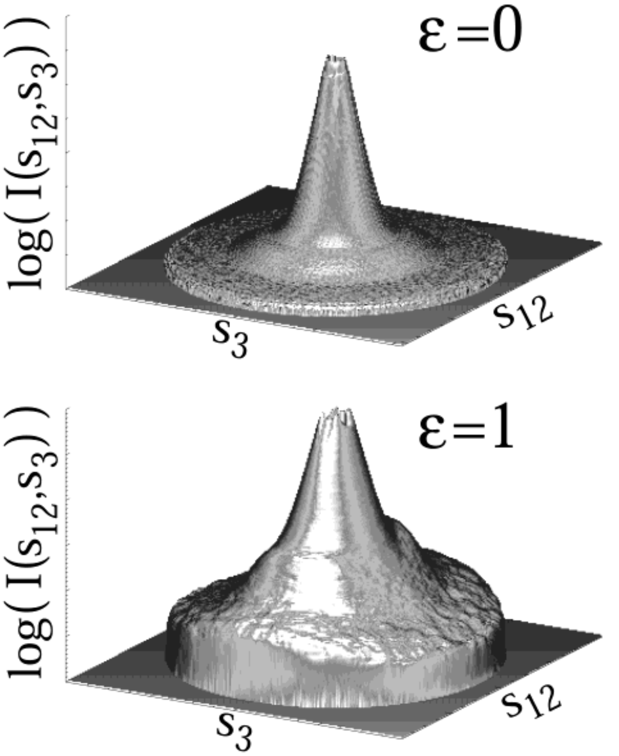

Figure 14. SAXS intensity $I(s_{12},s_3)$ (-0.4 nm$^{-1} \leq s_{12}, s_3 \leq 0.4$ nm^{-1}) of 53PTMeO/PA12 film cast from cyclohexanol after severe smoothing.

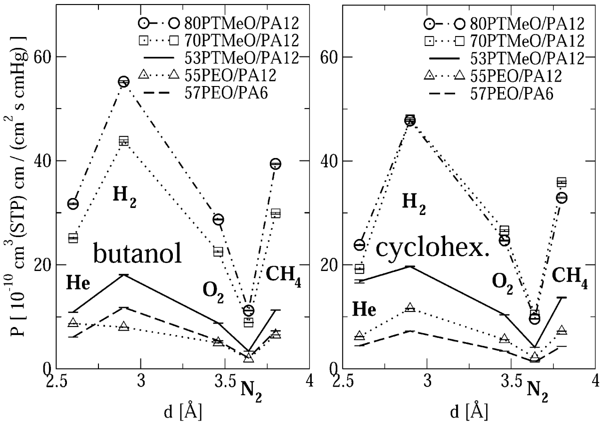

Figure 15. Permeabilities, *P*, of various gases for different PEBA membranes as a function of molecule diameter, *d*. Left: films cast from 1-butanol. Right: films cast from cyclohexanol.

Gas Transport Properties. Figure 15 shows measured permeabilities, *P*, as a function of gas molecule diameter for various gases and different PEBA grades. Results of films cast from 1-butanol are reported in the left diagram. The diagram on the right shows data for films cast from cyclohexanol. For the reason for keeping the drawings clear, the extremely high permeabilities for CO_2 are given in an extra table (cf. Table 5). Let us compare our results to published data[32] of films cast from 1-butanol that were determined in similar experiments. From 12 values measured in both studies, eight values are close to each other, and four values deviate considerably: our 57PEO/PA6 film shows double the permeability for CO_2, our 53PTMeO/PA12 material

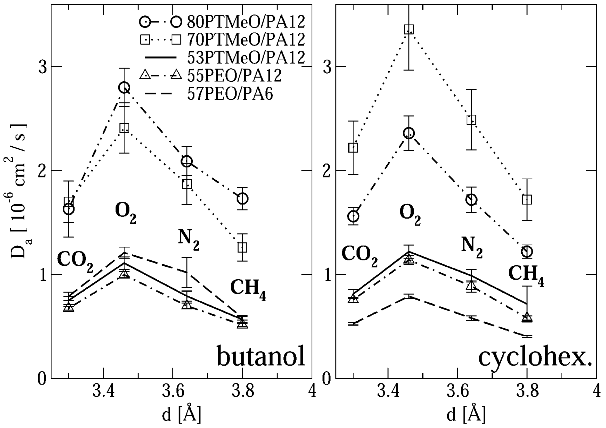

Figure 16. Apparent diffusion coefficients, D_a, of various gases through different PEBA membranes as a function of molecule diameter, *d*. Left: films cast from 1-butanol. Right: films cast from cyclohexanol.

Table 5. Permeabilities, *P*, of CO_2 for Different PEBA Grades; Films Cast from 1-Butanol and Cyclohexanol

	P [10^{-10} cm^3(STP) cm/(cm^2 s cmHg)]	
material	1-butanol	cyclohexanol
80PTMeO/PA12	276 ± 9	241 ± 6
70PTMeO/PA12	204 ± 13	256 ± 15
53PTMeO/PA12	81 ± 2	95 ± 2
55PEO/PA12	94 ± 1	106 ± 2
57PEO/PA6	109 ± 3	71.4 ± 0.8

shows half the permeability for H_2 but almost double the permeability for N_2, and our 80PTMeO/PA12 shows a considerably higher permeability for CO_2. We feel unable to explain the differences because permeability for different gases measured with one and the same membrane leads to agreement for some gases, whereas there is disagreement for others.

Our results confirm that the permeability is predominantly determined by the ratio of soft and hard blocks.[3] The samples with a high fraction of soft blocks exhibit the highest permeabilities. Lower permeabilities are shown by PEBA grades with a soft/hard composition close to 50/50. Moreover, exchanging the solvent from 1-butanol to cyclohexanol appears to reduce permeability of the grades 80PTMeO/PA12 and 57PEO/PA6, whereas the corresponding values for the 53PTMeO/PA12 are increased. The increase of the latter values corresponds to the observed strong increase of the average soft layer thickness observed with this material. With the 57PEO/PA6 we observe a constant soft layer thickness, but a decreased hard layer thickness with the sample cast from cyclohexanol. The decrease of permeability with this material may thus be explained by an increased soft domain density due to some hard blocks incorporated in the soft domains (poorer phase separation). This explanation is supported by the assessment based on the comparison of the scattering power *Q* (cf. Table 3). Both the materials with lowered permeability show a considerable decrease of SAXS scattering power. Concerning the poorly structured material 55PEO/PA12, only the H_2 permeability is seriously affected by changing the casting solvent. Altogether these findings support the notion that not only for polyurethane[4] but also for PEBA imperfect phase separation is decreasing permeability.

Figure 16 shows the apparent diffusion coefficients of different gases. Values for the small molecules He and H_2 have been omitted because of their low significance of determination. Again, the materials with a high soft block fraction show high values, and the poorly structured material 55PEO/PA12 is not affected by switching from 1-butanol to cyclohexanol. The diffusivity decrease for the materials 80PTMeO/PA12 and 57PEO/PA6 coincides with an imperfect phase separation (cf. Table 3). On the other hand, the considerable increase of the diffusion coefficients for 70PTMeO/PA12 cannot be explained by studied nanostructural features.

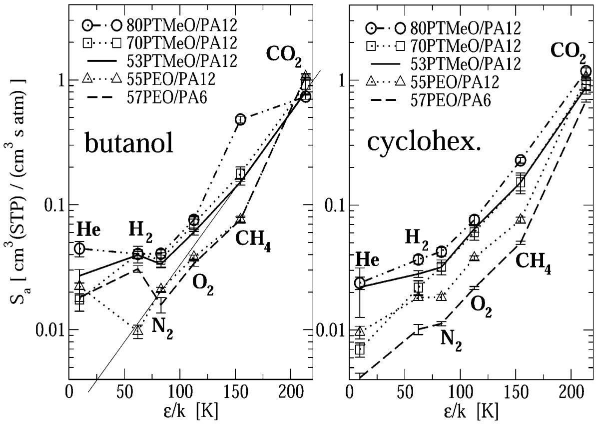

Figure 17. Apparent solubilities, S_a, of various gases through different PEBA membranes as a function of penetrant condensability measured in units of their Lennard-Jones temperature, ϵ/k. Left: films cast from 1-butanol. Right: films cast from cyclohexanol. The regression line for 57PEO/PA6 reported in ref 32 is indicated by a thin solid line crossing the left graph.

Apparent solubilities, S_a, as computed from permeabilities and diffusivities, are shown in Figure 17. They are presented in a half-logarithmic plot as a function of penetrant condensability, as has been proposed by Bondar, Freeman, and Pinnau[33] in a study of almost the same series of materials, but a direct method of solubility determination. Penetrant condensability is measured in units of the well depth of their Lennard-Jones potential, ϵ, divided by Boltzmann's constant, k.

Utilizing our indirect solubility determination, we obtain noisy data that do not permit to confirm the linear relationships established by Bondar, Freeman, and Pinnau for their membranes cast from 1-butanol. Nevertheless, the mutual arrangements of the curves in the diagram from top to bottom are the same. The solubilities measured in our low-pressure experiment for molecule sizes > H_2 are somewhat lower than the solubilities reported in the high-pressure experiment by Bondar et al.[33]

Conclusions

We have studied the nanostructure of different PEBA membrane materials and found that the domain diameters of the hard domains are almost the same for all the studied materials. By exchanging the casting solvent, the domain structure can easily be varied for the materials with almost 50% hard block content, whereas the materials with a low hard block content appear to reproduce an almost constant domain topology (size and arrangement of domains). If a considerable increase of the soft domain size is observed, an improvement of gas transport can be observed. Even if the domain topology is preserved when the casting solvent is exchanged, the perfection of phase separation may differ. Based on the results of the SAXS experiments, there are strong indications that samples with poor phase separation show decreased gas permeability and diffusivity.

Acknowledgment. Support of this work by GKSS project 6.T3.00.G.01.-HS1 and HASYLAB project II-01-041 is gratefully acknowledged.

References and Notes

(1) Dennis, G. M.; O'Brien, G. *Polyether Block Amide Resins: Bridging the Gap between Thermoplastics and Rubbers*; ACS Rubber Division Meeting Cincinnati; ATOFINA Chemicals Inc.: Philadelphia, Oct 2000.

(2) Bondar, V. I.; Freeman, B. D.; Pinnau, I. *Proc. Am. Chem. Soc. PMSE Prepr.* **1997**, *77*, 311.

(3) Kim, J. H.; Ha, S. Y.; Lee, Y. M. *J. Membr. Sci.* **2001**, *190*, 179.

(4) Damian, G.; Espuche, E.; Escoubes, M.; Cuney, S.; Pascault, J. P. *J. Appl. Polym. Sci.* **1997**, *65*, 2579.

(5) Drzal, P. L.; Halasa, A. F.; Kofinas, P. *Polymer* **2000**, *41*, 4671.

(6) Chew, C. H.; Li, T. D.; Gan, L. H.; Quek, C. H.; Gan, L. M. *Langmuir* **1998**, *14*, 6088.

(7) Miyata, T.; Obata, S.; Uragami, T. *Macromolecules* **1999**, *32*, 3712.

(8) Premnath, V. *J. Membr. Sci.* **1996**, *110*, 133.

(9) Shilton, S. J.; Bell, G.; Ferguson, J. *Polymer* **1996**, *37*, 485.

(10) McLean, R. S.; Sauer, B. B. *J. Polym. Sci., Part B: Polym. Phys.* **1999**, *37*, 859.

(11) Wu, D. Q.; Liang, B.; Hsiao, B. S.; Li, Y.; Chu, B. *Polym. Prepr. (Am. Chem. Soc., Div. Polym. Chem.)* **1992**, *33*, 350.

(12) Grigoriew, H.; Chmielewski, A. G. *J. Membr. Sci.* **1998**, *142*, 87.

(13) Ruland, W. *Colloid Polym. Sci.* **1977**, *255*, 417.

(14) Grigoriew, H.; Wolinska-Grabczyk, A.; Chmielewski, A. G.; Amenitsch, H.; Bernstorff, S. *J. Membr. Sci.* **2000**, *170*, 275.

(15) Elliott, J. A.; Hanna, S.; Elliott, A. M. S.; Cooley, G. E. *Macromolecules* **2000**, *33*, 4161.

(16) Gebel, G.; Lambard, J. *Macromolecules* **1997**, *30*, 7914.

(17) Gebel, G. *Polymer* **2000**, *41*, 5829.

(18) Stribeck, N. *J. Appl. Crystallogr.* **2001**, *34*, 496.

(19) Stribeck, N.; Buzdugan, E.; Ghioca, P.; Serban, S.; Gehrke, R. *Macromol. Chem. Phys.* **2002**, *203*, 636.

(20) Stribeck, N.; Fakirov, S.; Sapoundjieva, D. *Macromolecules* **1999**, *32*, 3368.

(21) Buhmann, M. D. *Acta Numerica* **2000**, *9*, 1.

(22) Stribeck, N. *Colloid Polym. Sci.* **2002**, *280*, 254.

(23) Vonk, C. G. *Colloid Polym. Sci.* **1979**, *257*, 1021.

(24) Ruland, W. *Colloid Polym. Sci.* **1978**, *256*, 932.

(25) Stribeck, N.; Ruland, W. *J. Appl. Crystallogr.* **1978**, *11*, 535.

(26) Flores, A.; Pietkiewicz, D.; Stribeck, N.; Roslaniec, Z.; Baltá Calleja, F. J. *Macromolecules* **2001**, *34*, 8094.

(27) Stribeck, N. *Colloid Polym. Sci.* **1993**, *271*, 1007.

(28) Stribeck, N. *J. Phys. IV* **1993**, *3*, 507.

(29) Stribeck, N.; Wutz, C. *Macromol. Chem. Phys.* **2002**, *203*, 326.

(30) Fronk, W.; Wilke, W. *Colloid Polym. Sci.* **1985**, *263*, 97.

(31) Stribeck, N. *ACS Symp. Ser.* **2000**, *739*, 41.

(32) Bondar, V. I.; Freeman, B. D.; Pinnau, I. *J. Polym. Sci., Part B: Polym. Phys* **2000**, *38*, 2051.

(33) Bondar, V. I.; Freeman, B. D.; Pinnau, I. *J. Polym. Sci., Part B: Polym. Phys.* **1999**, *37*, 2463.

MA0213403